Designing the Actuator for the Next-Generation Astronomical Deformable Mirrors: a Multidisciplinary and Multiphysics Approach

C. Del Vecchio*,[1], R. Biasi[2], A. Riccardi[1], and D. Gallieni[3]
[1]INAF-OAA, [2]Microgate Srl, [3]ADS International SrL
*L. Enrico Fermi 5 I-50125 Firenze, cdelvecchio@arcetri.astro.it

Abstract: The actuation system of the deformable mirror is one of the crucial components of an Adaptive Optics unit. One possible implementation comprehends a linear force motor and a capacitive sensor providing the feedback measure signal. Choosing a magnetic circuit that makes optimum use of the magnetic force delivered by a current and properly arranging the electrostatic geometry allows to obtain very good results. This paper, after a description of the magnetic design, discusses the mutual relationships in the physics of the device: as the magnetostatic and thermal responses as well as the fluid dynamics in the physical implementation interact, such computations are carried out in order to define the thermal impact of the actuator on the local environment as a function of the delivered force.

Keywords: Adaptive Optics, Electromagnetism, Actuator, Fluid Dynamics, FEA

1 Introduction

Coupling an electromagnetic linear motor with a capacitive sensor providing the measuring feedback signal allows to reach the high performances of the large deformable mirrors (DM) of the modern Adaptive Optics (AO) systems. Figure 1 shows the principle of operation the closed loop system. The turbulence sensed by the wavefront sensor is corrected by the actuators that apply some displacements to the DM, in order to flatten the wavefront. Provided that the force actuator is efficient in terms of delivered force versus required power and the capacitive sensor is accurate enough to provide the actuator with the proper position reading, the control system of the closed loop motor is able to correct the atmospheric turbulence within the (very severe) specifications of the current and future generation telescopes. Such instruments, as the Large Binocular Telescope (LBT) and the Multiple Mirror Telescope (MMT), are equipped with secondary deformable mirrors actuated with voice-coil type linear motors which allow contact-less motions of the DM with the nanometer accuracy thanks to the feedback capacitive sensor coaxial with the actuator. As described in [1] and [2], the force is developed by circulating a current in a coil facing a coaxial, radially magnetized toroidal permanent magnet, possibly retro-fitted with an axially polarized magnet, as described in [4]. Although such a design greatly simplifies both the mechanics (the statoric and moving parts are fully decoupled and the total mass is quite low) and the magnetic circuit of the actuator (no iron is needed), it cannot exhibit efficiencies greater than $\approx .7\,\mathrm{N} \times \mathrm{W}^{-\frac{1}{2}}$ and the proximity of the capacitive sensor to the permanent magnet may require some shielding of the sensor itself. Because a high-order, large-thickness and long-stroke adaptive telescope mirror is desirable in the optical design of the Extremely Large Telescopes (ELT), a different approach has been developed, in order to increase the efficiency, so avoiding any thermal pollution in the very delicate optical environment. Moreover, the development of a more efficient kind of actuators represents a spin-off for adaptive segments of primary mirrors.

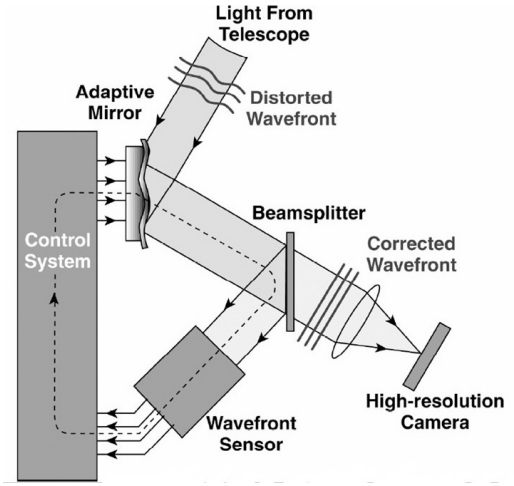

Figure 1: Conceptual scheme of an Adaptive Optics System.

This paper deals with the variable reluctance linear motor described in [3]. The promising results of the electromagnetic model based on that concept have led to a complete design, which, in turn, has allowed to build a full scale prototype of the actuator. The rationale of the actuator able to fulfill the requirements listed in table 1 is discussed in Section 2 along with the modeling criteria. Section 3 describes the implementation of the multiphysics problem, and Section 4 the relative results.

rms force (turb. corr.) [N]	.363
max force (static) [N]	.36
max force (dynamic) [N]	1.27
stroke [μm]	±150
bandwidth [kHz]	1
typical actuator spacing [mm]	25
typical mover mass [g]	≤ 10
resistance [Ω]	2 to 2.5
measuring range [μm]	±100
resolution [nm]	< 3
rms noise [nm]	< 5
drift[a] [nm]	20
bandwidth [kHz]	> 30

Table 1: Basic requirement of the actuator for the high order DM

[a] 12 hrs base, 5°C temperature variation

2 The actuator

2.1 The multiphysics problem

The optimization process of the magnetic circuit described in [3] and schematized in figure 2 has provided the actuator depicted in figure 3, where the relevant components are highlighted.

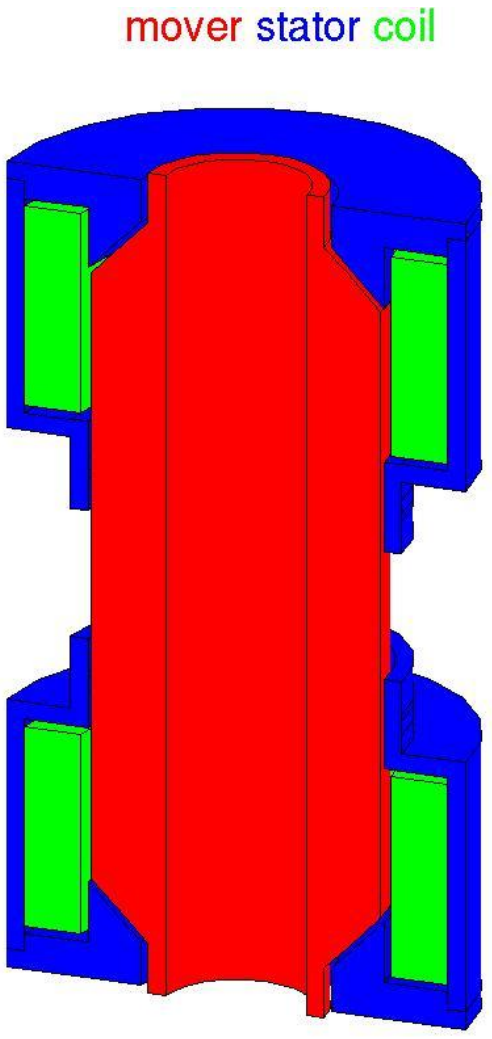

Figure 2: Scheme of the magnetic circuit. The current that circulates (green) coil produces a magnetic flux density which is concentrated in the stator iron (blue) and mover iron (red), so that on the latter a magnetic force is applied (see [3] for a discussion).

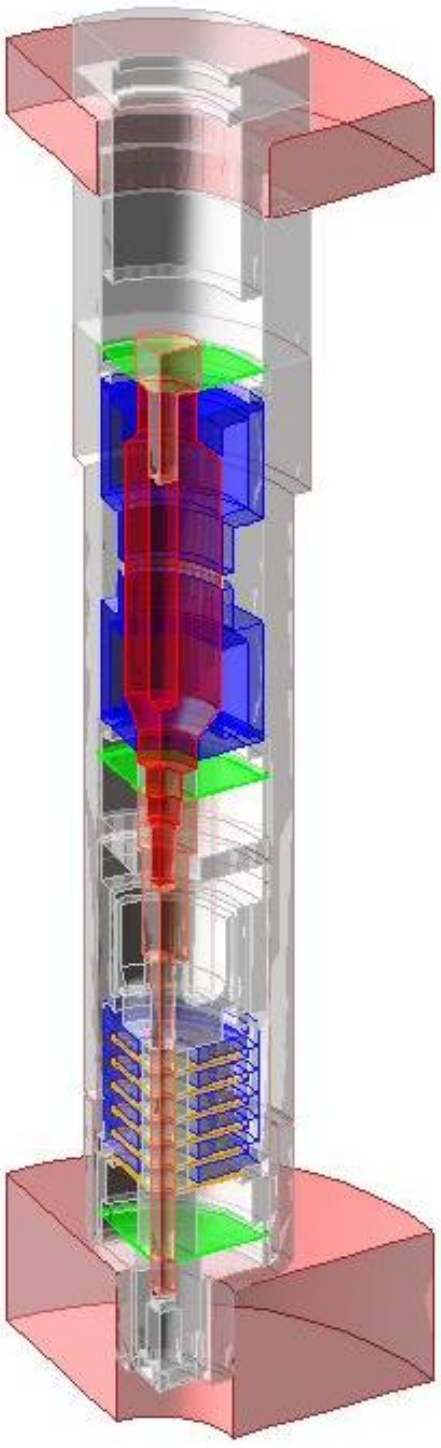

Figure 3: Overall scheme of the actuator. The main moving components are red and orange (mover, shaft, and capacitive sensor moving armatures, from top to bottom); the main static components are blue and light blue (stator and capacitive sensor fixed armatures, from top to bottom); the membranes are green; the reference frame (bottom) and the aluminum plate are purple.

A Macor shaft, bolted to the optimized iron core, accommodates the six mobile armatures of the capacitive sensors, providing the required axial stiffness. The shaft hosts the permanent magnet aimed to provide the magnetic link with the DM (not shown), via an iron sphere. The mobile armatures and their correspondent fixed counterparts, rigidly connected to the actuator body, make up the capacitive sensor. The above mentioned actuator body accommodates also the statoric iron components as well as the coils of the magnetic circuit. The body is bolted to the bottom SiC reference frame and clamped to the top aluminum plate. The mobile and the fixed parts are connected via three thin titanium membranes, that provide a high in-plane stiffness while they are very weak in the axial direction.

The power dissipated by the coil is to be conveyed to an heat sink avoiding that the temperature of any point of the external surface of the actuator exceeds the reference temperature T_{ref} by $\pm 1\,\mathrm{K}$, according to the specifications. We propose two solutions. In the first one, named *active*, a suitable coolant flows in some holes drilled in the top aluminum plate (as a first attempt, four circular channels of radius $.75\,\mathrm{mm}$), the second one, named *passive*, relies only on the air, supposed to be able to remove the heat by natural convection. In both cases, two input currents are considered, the ones corresponding to the turbulence correction force and the maximum dynamic force defined in table 1. As the goal of the analysis is the stationary power budget, only the steady-state solutions are computed.

2.2 The model

Besides these basic components described in section 2.1, all the other auxiliary parts, supports, shims, spacers, washers, bushes, screws, and the electronics board, have been imported into Comsol Multiphysics via the *CAD Import Module* in order to generate the geometry in the the r–z coordinate system, as the actuator is basically axially symmetric and the purpose of this study is the evaluation of a single actuator thermal response. That geometry has been meshed very finely in the air gap and coil areas, so that the magnetic and the thermal responses could

be properly computed — as discussed in [3], the stator-mover air gap and the wire insulation thickness are as small as 200 and 7 µm, respectively. The resulting mesh consists of $\approx 55,000$ points and $\approx 100,000$ elements, .5% of which have a quality $\leq .4$ — with a minimum quality of .19.

3 The application modes

3.1 Magnetostatics

The computation of the magnetic force, defined as $\mathbf{F} = \int_V (\mathbf{M} \cdot \nabla)\, \mathbf{B}\, dV$, is based on the calculation of the Maxwell stress tensor, as discussed in [3]. Because of the coupling with the heat transfer application mode discussed in section 3.2, the coil — 138 circular copper wires, arranged in a 23 by 6 rectangular pattern, whose overall radius is .1195 mm, including the 7.5 µm thick polyimide insulation — is fully modeled, and the copper conductivity is defined as $\sigma_{Cu} = 1/(\rho_{Cu_{ref}} \times (1+0.0039 \times (T-293)))$ S × m^{-1}, where $\rho_{Cu_{ref}} = 1.72 \times 10^{-8}\,\Omega \times \mathrm{m}$ is the copper resistivity at 293 K, in order to consider the resistivity variation when the temperature T changes.

3.2 Heat transfer

The heat transfer is computed neglecting the radiative contribution — the expected temperature differences are very low. Furthermore, only the air subdomains not trapped in the solid subdomains are supposed to be affected by convection — i.e. the convection is enabled only for those air subdomains that are bounded by the most outer boundaries. In such subdomains the density is defined assuming that the air is an ideal gas, whose equation of state is $pV = nRT$. As the number of moles n is equal to m/M, where $M = 28.97 \times 10{-}3\,\mathrm{kg} \times \mathrm{mol}^{-1}$ is the air molar mass and $R = 8.314472\,\mathrm{J} \times \mathrm{mol}^{-1} \times \mathrm{K}^{-1}$ is the universal gas constant, the air density is defined by equation 1, where the pressure p is computed by the application mode defined in section 3.3. Also the air velocity, whose r and z components are u and v, respectively, is computed in the application mode defined in section 3.3.

$$\rho_{air} = \frac{M}{R}\frac{p}{T} = 3.484 \times 10^{-3}\frac{p}{T} \quad [\mathrm{kg} \times \mathrm{m}^{-3}] \quad (1)$$

In order to simulate the contribution of the surrounding actuator and the environment, the boundary conditions are set as $T = T_{ref} = 293\,\mathrm{K}$ on the bottom, horizontal boundary — the interface with the air gap trapped between the SiC reference frame and the DM, not modeled — , as thermal insulation on the outer vertical one limiting the domain at one half of the actuator separation ($r = 12\,\mathrm{mm}$) — the interface with the contiguous actuator domain — and as a convective flux on the top, horizontal one — the interface with the ambient air. In the *active* model defined in section 2.2 the circumferential boundaries of the coolant domain are set to $T = T_c$ — the input coolant temperature.

3.3 Fluid dynamics

The weakly compressible Navier-Stokes application mode, active only for the air subdomains where the convection is enabled, according to section 3.2, is based on the density defined in equation 1, the dynamic viscosity defined in equation 2 as a function of T, and the volume force defined in equation 3, where ρ_{ref} is computed setting $T = T_{ref}$ and $p = p_{atm} = 101325\,\mathrm{Pa}$ — the average (sea-level) pressure of the air — in equation 1.

$$\begin{aligned} \eta \;=\; & -7.887 \times 10^{-12}\,T^2 + \\ & 4.427 \times 10^{-8}\,T + \\ & 5.204 \times 10^{-6} \quad [\mathrm{Pa} \times \mathrm{s}^{-1}] \end{aligned} \quad (2)$$

$$f_z = 9.81\ (\rho_{ref} - \rho_{chns}) \quad [\mathrm{N} \times \mathrm{m}^{-3}] \quad (3)$$

The boundaries representing the interface with the solid subdomains are treated as boundaries where u and v are 0, while on the ones identified by the thermal insulation, defined in section 3.2, $\mathbf{n} \cdot [u; v] = 0$ is set as boundary condition; the top boundary is set as an outlet, i.e. a static pressure $p = p_{atm}$ is applied on such a boundary.

4 Results

The most relevant result from the electromagnetic standpoint is the map of the flux lines of the magnetic flux density, shown in figure 4. The optimized geometry of the magnetic circuit allows to obtain a suitable magnetic force. The ferromagnetic components embracing the magnet provide the magnetic force at the DM

interface, while avoiding any electromagnetic undesired effect in the capacitive sensor. Integrating the Maxwell stress tensor $\mathbf{T} = -\frac{1}{2}(\mathbf{H}\cdot\mathbf{B})\,\mathbf{n} + (\mathbf{n}\cdot\mathbf{H})\,\mathbf{B}^T$ on the mover surface gives the axial force F_z, the z component of $\mathbf{F}$, and integrating the product $J^2\,\rho$, where J is the current density and $\rho = \rho(T)$ is the copper resistivity gives the dissipated power P, respectively. Computing the efficiency $\epsilon = F_z/P$ in the *active* (with $T_c = T_{ref}$) and *passive* models shows that $4.05 \leq \epsilon \leq 4.1\,\mathrm{N}\times\mathrm{W}^{-1}$ — such a small variation is due to the fact that the temperature increase in the copper ΔT_{cu} is quite low: from .57 to 3.98 K, pending on the model. Considering $\epsilon = 4.075\,\mathrm{N}\times\mathrm{W}^{-1}$ as the average efficiency and $R = 2\,\Omega$ as the nominal resistance (see [3]), the currents giving the maximum dynamic force and the rms correction force listed in table 1 are .38 and .21 A, respectively. Comparing the power required by such an efficient actuator to deliver a given force with the power required by the LBT actuator, whose efficiency is $.622\,\mathrm{N}\times\mathrm{W}^{-1/2}$ (see [1]), to deliver the same force, it turns out that the dissipation of the latter if greater than the one of the former by a factor of 13.3 for a 1.27 N force and by a factor of 2.6 for a .25 N force.

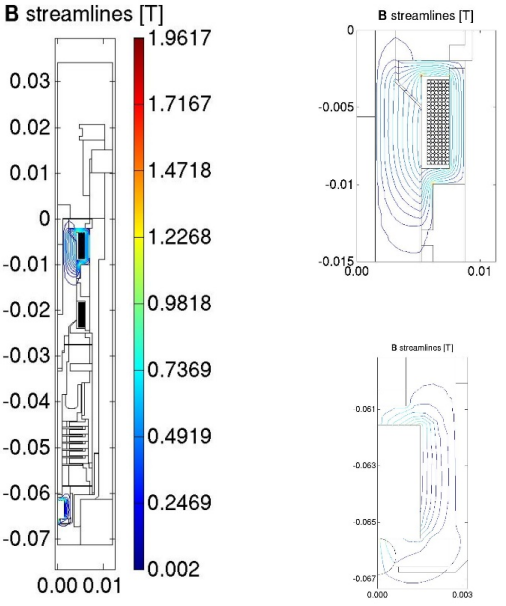

Figure 4: Flux lines of $\mathbf{B}$ (left). As they are concentrated around the coil and the magnet, such areas are plotted in the right top and right bottom, respectively.

As the stiffness of the DM is proportional to the third power of its thickness and inversely proportional to the fourth power of the actuator spacing, such a stiffness is incremented by a factor of two either reducing the spacing by only 16% — the difference between the actuator distance listed in table 1 and the correspondent LBT DM value — and increasing the DM thickness by only 20% — the typical increasing of the ELT primary mirror panel thickness with respect to the mean LBT DM thickness, 1.6 mm. Therefore, even if more mechanically complex, the much more efficient variable reluctance motor is much more suitable for the modern AO techniques.

Non-linearly solving for the *active* model as a function of the coolant temperature $T_c = T_{ref} - \Delta T_c$, it turns out that $\Delta T_c = 0$ gives the lowest outer temperatures of the actuator. Although $\Delta T_c < 0$ allows to obtain a slightly lower power dissipation, as the copper reaches temperatures slightly lower than in the $\Delta T_c = 0$ condition, the latter is selected as the optimal active cooling system. In fact, with maximum $\Delta T = T - T_{ref}$ of .35 and .1 K when the maximum dynamic force and the rms correction forces are applied (see figure 5), the $\Delta T_c = 0$ condition largely satisfies the specifications.

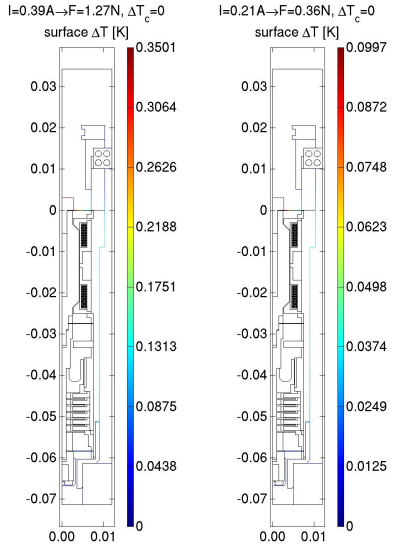

Figure 5: Active cooling: temperature distribution on the actuator outer surface.

The maximum ΔT obtained by solving the simpler *passive* model with the currents giving the above mentioned forces are $\Delta T = T - T_{ref}$ of 2.24 and .64 K, respectively (see figure 6). Although the *passive* model does not fulfill the specification when the maximum dynamic force is applied — indeed, a very rare case in the telescope operational modes — this cooling scheme, much simpler than the *active* one, is worthy of further analyses. In fact, due the boundary condition $T = T_{ref}$ on the bottom boundary, that implies an heat flux towards the small air gap between the reference frame and the DM, the capability of the gap to convey such a flux should be verified. For this reason, the results of the *passive* model have to be regarded as a first approximations ones — a model including the air gap and the DM, with a convective boundary condition on the bottom of the DM itself, is on the way.

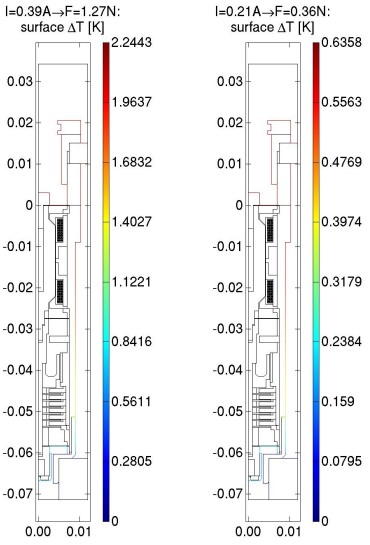

Figure 6: Pure convection cooling: temperature distribution on the actuator outer surface.

Figure 7 shows the air velocity stream lines for both the *active* (left) and *passive* (right) models, when the actuator is applying the maximum dynamic force. The maximum velocities are .1 and .045 mm $\times$ s^{-1}, respectively.

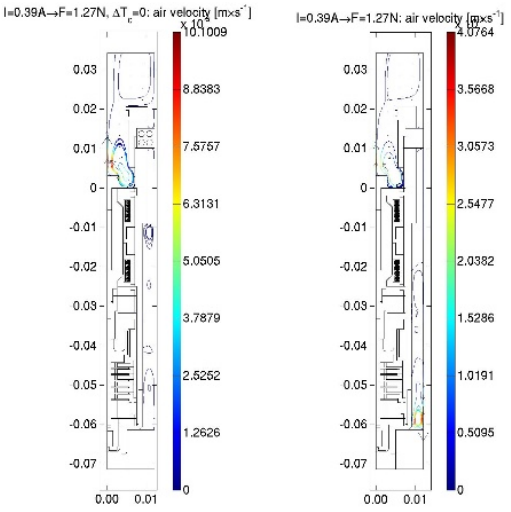

Figure 7: Velocity field in the air domain (see text for a discussion).

5 Tests and plans

The actuator prototype, whose components are shown in in figure 8, is currently undergoing the preliminary tests. In spite of the very good mechanical and electrostatic test results, the measured efficiency is quite lower than the design figure — probably because of the slightly mismatching at the interface between the two statoric subcomponents and the filling factor of the coil. A revision of the manufacturing of such parts is on the the way.

Figure 8: The actuator prototype.

As mentioned in Section 3.2, we assume that the boundary condition at the most outer vertical boundary matches the geometrical symmetry of the model. Actually, as the actuators of the AO unit are not arranged with such a symmetry, the results of the 2d model have to be verified by means of a 3d, simplified model, in order to evaluate

the thermal interaction between actuators. A 3d model containing the outer surface of several actuators, each one with the temperature distribution computed with 2d model applied on those surfaces, is planned.

Furthermore, the efforts spent in developing a 3d model of the electromagnetic portion of the single actuator in order to compute the effects of small displacements and/or rotations of the mover — basically, the calculation of the forces in the plane normal to the actuator axis and the relative torque, which are quite small, according to the electromagnetic 3d results — have to be extended to the electrostatic 2d computations discussed in [3].

Finally, besides the improvements mentioned in Section 4, we have planned to add an axial symmetry, stress-strain application mode to the current application modes, in order to verify that the thermal deformations do not affect significantly the gaps relevant for the magnetic force and for the capacitive sensor stages.

6 Conclusion

The more and more demanding Adaptive Optics techniques will require both high-order deformable mirrors, with actuator densities larger than the current ones, and low-order deformable mirrors thicker than the present ones. As a consequence, the diameter of the current actuators have to be reduced and their efficiency must be increased. The encouraging results obtained with the variable reluctance motor allowed to build a prototype whose computed efficiency is slightly greater than $4\,\mathrm{N} \times \mathrm{W}^{-1}$, thanks to some optimization. The heat transfer of such a complex device has been computed with two approaches, with and without an active cooling system, in order to identify a solution able to minimize the impact on the delicate telescope environment. Both of them exhibit advantages and disadvantages, discussed in this paper, in order to choose the configuration able to fulfill the requirements at reasonable costs.

References

[1] G. Brusa, D. L. Miller, M. Kenworthy, D. Fisher, and A. Riccardi, *MMT-AO: two years of operation with the first adaptive secondary*, Advancements in Adaptive Optics (Glasgow, UK) (Domenico Bonaccini Calia, Brent L. Ellerbroek, and Roberto Ragazzoni, eds.), vol. 5490, SPIE, 6 2004, pp. 23–33.

[2] C. Del Vecchio, *Supporting a magnetically levitated, very thin meniscus for an adaptive secondary mirror: the optimization of the magnetic circuit*, Adaptive Optics and Applications (San Diego, CA) (Robert K. Tyson and Robert Q. Fugate, eds.), vol. 3126, 7 1997, pp. 605–613.

[3] C. Del Vecchio, R. Biasi, D. Gallieni, A. Riccardi, and R. Spairani, *Actuating the deformable mirror: a multiphysics design approach*, Advanced Optical and Mechanical Technologies in Telescopes and Instrumentation (Marseille, France) (Eli Atad-Ettedgui and Dietrich Lemke, eds.), vol. 7018, SPIE, 6 2008, pp. E.1–E.11.

[4] C. Del Vecchio, G. Gallieni, H. M. Martin, A. Riccardi, G. Brusa, and R. Biasi, *Design improvements of the LBT adaptive secondary*, Beyond Conventional Adaptive Optics (Venice, Italy) (Elise Vernet, Roberto Ragazzoni, Simone Esposito, and Norbert Hubin, eds.), vol. 58, ESO, 5 2001, pp. 435–441.

Acknowledgements

The authors would like to thank Dr. Samuele Piazzini from Department of Energy Engineering, Florence University, Italy, for insight and guidance through the Navier-Stokes application mode for which we are grateful. Part of this research was supported by the FP6 funds (ELT design study project, WP9300, Contract RIDS-011863), received from EU.